Scalable Learning-Based Sampling Optimization for Compressive Dynamic MRI

Thomas Sanchez[1], Baran Gözcü[1], Ruud B. van Heeswijk[2], Efe Ilıcak[3], Tolga Çukur[3,4], and Volkan Cevher[1]
[1]Laboratory for Information and Inference Systems (LIONS), EPFL, Switzerland
[2] Center for BioMedical Imaging (CIBM), Department of Radiology, CHUV, Switzerland
[3]National Magnetic Resonance Research Center (UMRAM), Bilkent University, Ankara, Turkey
[4]Department of Electrical and Electronics Engineering, Bilkent University, Ankara, Turkey

Slow acquisition has been one of the historical problems in dynamic magnetic resonance imaging (dMRI), but the rise of compressed sensing (CS) has brought numerous algorithms that successfully achieve high acceleration rates. While CS proposes random sampling for data acquisition, practical CS applications to dMRI have typically relied on random variable-density (VD) sampling patterns, where masks are drawn from probabilistic models, which preferably sample from the center of the Fourier domain. In contrast to this model-driven approach, we propose the first data-driven, scalable framework for optimizing sampling patterns in dMRI. Through a greedy algorithm, this approach allows the data to directly govern the search for a mask that exhibits good empirical performance. Previous greedy approach, designed for static MRI, required very intensive computations, prohibiting their direct application to dMRI, and we address this issue by resorting to a stochastic greedy algorithm that exploits only a fraction of resources compared to the previous approach without sacrificing the reconstruction accuracy. A thorough comparison on *in vivo* datasets shows the inefficiency of model-based approaches in terms of sampling performance and suggests that our data-driven sampling approach could fully enable the potential of CS applied to dMRI.

***Index Terms*—Dynamic magnetic resonance (MR) imaging, compressive sensing (CS), learning-based sampling, greedy algorithms**

I. Introduction

DYNAMIC Magnetic Resonance Imaging (dMRI) is a powerful tool in medical imaging, which allows for non-invasive anatomical or functional monitoring of tissues over time. A main challenge to the quality of dMRI examinations is the inefficiency of data acquisition that limits temporal and spatial resolutions. In the presence of moving tissues, such as in cardiac MRI, the trade-off between spatial and temporal resolution is further complicated by the need to perform breath holds to minimize motion artifacts. [1].

In the last decade, the rise of Compressed Sensing (CS) has significantly contributed to overcoming these problems. CS allows for a successful reconstruction from undersampled measurements, provided that the data can be sparsely represented in some domain and that the measurements are incoherent [2], [3]. In dMRI, samples are acquired in the k-t space (spatial frequency and time domain), and the temporally neighboring images are highly correlated, which enables the signal to be sparsely represented in the x-f domain (image and temporal Fourier transform domain). Many algorithms have exploited this framework with great success [4]–[16]. Some works also exploit dictionary learning, where they design a compact sparsifying transform [17]–[19], and some focus on low-rank approaches [8], [15], [20], [21].

While CS theory mostly focuses on fully random measurements [22], the practical implementations have generally exploited *random variable-density sampling*, based on drawing random samples from a parametric distribution which reasonably imitates the energy distribution in the k-t space. This was proposed by Lustig et al. for static MRI [23], and applied to dMRI by Jung et al. [24]. A few works later specifically attempted at designing sampling patterns for dMRI [25], [26].

While all these approaches allow to quickly design masks which yield a great improvement over fully random sampling, prescribed by the theory of CS, they remain fully heuristic and ignore the anatomy and the reconstruction algorithm at hand. In the present study, we propose a *scalable learning-based framework* for dMRI that, given a reconstruction algorithm, allows the data to drive the design of the sampling pattern. The present work extends the work of Gözcü et al. [27] for MRI, where they proposed a greedy method exploiting fully-sampled training data, which has the advantage of being practical, flexible, as well as theoretically grounded.

The principle behind the greedy method is the following: We start from an empty mask, compute how much adding each phase encode (horizontal line of points in Fourier space) separately to the mask increases the quality of the reconstruction over some training images with respect to a performance metric (e.g. PSNR), and pick the phase encode which maximizes it. We keep iterating on all phase encodes not yet added to the mask up to a maximal cost (e.g 30% sampling rate). Gözcü's approach typically uses all of the phase encodes at each iteration, which does not generalize well to dMRI due to the larger dimension of the data. The proposed stochastic greedy algorithm solves this issue by exploiting a fraction of the phases encodes at each iteration, while achieving a similar reconstruction quality, but with a *drastic runtime improvement*.

Numerical evidence shows that our framework can successfully find sampling patterns for a broad range of decoders, from k-t FOCUSS [6] to iterative soft-thresholding [12] and ALOHA [21], outperforming state-of-the-art model-based sampling methods, relying on coherence minimization or parameter tuning, over nearly all sampling rates considered. Although we focused on single-coil Cartesian dynamic dMRI in the present study, our method can readily be generalized to parallel imaging as well as non-Cartesian setups.

Outline of the paper: In Section II, we introduce the

Submitted to IEEE Transactions on Medical Imaging on July 25, 2018; revised December 12, 2018; rejected January 17, 2019.

CS formulation for dMRI, detail the most relevant existing reconstruction algorithms and sampling methods and we highlight our contribution. In the following Section III, we summarize the learning-based framework of [27] and introduce our scalable learning-based algorithm. Then, in Section IV, we demonstrate the benefits of the scalable approach against the framework of [27], and proceed to show the effectiveness of our method compared to the existing approaches on several *in vivo* data sets. Conclusions are drawn in Section V.

II. Background

A. Problem formulation

In the compressed sensing (CS) problem [3], one desires to retrieve a signal that is known to be sparse in some basis using only a small number of linear measurements. In the case of dynamic MRI, we consider a signal $\mathbf{x} \in \mathbb{C}^{N\times N\times T}$ (i.e. a video of size $N \times N$ with T frames), which will be written on a vectorized form $\mathbf{x} \in \mathbb{C}^p$ for convenience, and we have subsampled Fourier measurements described as

$$\mathbf{b} = \mathbf{P}_\Omega \mathbf{\Psi} \mathbf{x} + \mathbf{w} \tag{1}$$

where $\mathbf{\Psi} \in \mathbb{C}^p$ is the spatial Fourier transform operator applied to the vectorized signal, $\mathbf{P}_\Omega : \mathbb{C}^p \to \mathbb{C}^n$ is a subsampling operator that selects the rows of $\mathbf{\Psi}$ according to the indices in the set $\mathbf{\Omega}$ with $|\Omega| = n$ and $n \ll p$. We refer to Ω as *sampling pattern* or *mask*. We assume the signal $\mathbf{x}$ to be sparse in the basis $\mathbf{\Phi}$, which typically is a temporal Fourier transform across frames [6], [12]–[16], [21]. Given the samples $\mathbf{b}$, along with Ω, a *reconstruction algorithm* or *decoder* g forms an estimate $\hat{\mathbf{x}}$ of $\mathbf{x}$ such that

$$\hat{\mathbf{x}} = g(\mathbf{b}, \Omega) \tag{2}$$

Many reconstructions have been proposed over the years, and we detail hereafter several state of the art methods that are considered in Section IV for single-coil datasets. An early approach for successful CS recovery in dynamic MRI is k-t FOCUSS [6], which approximates the result of the problem

$$\min_{\mathbf{x}\in\mathbb{C}^p} \|\mathbf{\Phi}\mathbf{x}\|_1 \text{ s.t. } \|\mathbf{P}_\Omega\mathbf{\Psi}\mathbf{x} - \mathbf{b}\|_2 \leq \epsilon. \tag{3}$$

A later method is the Iterative Soft-Thresholding (IST), which directly solves the problem (3) [12]. More recently, a generic framework for both single and multi-coil dMRI was developed named annihilating filter based low-rank Hankel matrix approach (ALOHA) by Jin et al. [21]. ALOHA exploits the duality between sparse signals and their transform domain representations cast as a low-rank Hankel matrix. This duality can be used to reformulate the CS recovery as a low-rank matrix completion problem.

Many other algorithms have been developed to solve the dynamic MRI problem with Cartesian sampling, and the first one to be used was k-t SPARSE [4], which solves the problem (3) with a conjugate gradient method. Other approaches combined low-rank and sparse approaches [8], [14], [15], or use dictionary learning to sparsely represent a signal [18], [19], [28], and more recently, deep learning reconstructions [16] have yielded promising results. While we primarily consider Cartesian dMRI here, non-Cartesian sampling based on radial trajectories has also been used broadly to enable free-breathing scans [13], [29].

B. Sampling mask design

The most widely used approach for the design of the sampling pattern $\mathbf{\Omega}$ is *random variable-density sampling*, which was originally proposed by Lustig et al. [23] for static MRI. It offers a compromise between incoherent measurements, required by the theory of CS, and the structure that can be found in the k-space, where most of the energy is concentrated in the low frequency end of the spectrum. This classical approach draws random samples according to a parametric distribution mimicking the energy distribution of the k-space, favoring low-frequency samples. The distribution considered is typically either polynomial [14], [23], [30], [31], or Gaussian [6], [7], [15], [16], [19], [21]. In these setups, a slight offset is often added in order to prevent the distribution from having extremely small probabilities at high-frequencies, and a few low-frequency k-space samples are acquired at the Nyquist rate.

The variable-density based methods commonly used in dMRI perform well, but have several weaknesses, already highlighted in [27] for static MRI. They require parameters to be tuned, such as decay rate of the polynomial, the standard deviation of the Gaussian distribution or the number of central phase encodes and arbitrarily constrain the sampling patterns to a model without any theoretical justification. Moreover, it is unclear which sampling density will be most effective for a given anatomy and reconstruction rule. Also, the idea of randomizing the acquisition is in itself questionable, as in practice, one would desire to design a fixed sampling pattern that we will know to perform well for a specific anatomy across many subjects. Finally, some variable-density methods, such as Poisson Disc Sampling [32], do not use a fixed number of readouts per frame, which complicates their hardware implementation for dynamic MRI [25]. Indeed, undersampling some frames more heavily than others might result in missing critical temporal information.

Recently, several articles have focused on improved design of spatiotemporal sampling patterns for dMRI, and we hereafter detail two particularly relevant methods. A recent state-of-the-art method devised for this purpose is the variable density incoherent spatiotemporal acquisition (VISTA) [25] that minimizes Riesz energy on a spatiotemporal grid, and has the notable advantage of generating patterns with high levels of incoherence, and maintaining uniform sampling density across frames. Another important technique proposed by Li et al. [26] develops a method for Cartesian sampling exploiting the golden-ratio, with the aim to generate incoherent measurements and maintain uniform sampling density across frames[1].

Other relevant undersampling works include, in the non-Cartesian setting, fully random radial sampling [14], [33], as well as golden-angle radial sampling, where spokes separated by the golden-angle are continuously acquired [13], [29], [34]. These results exploit the inherent advantage of radial over Cartesian sampling that each spoke goes through the sample of the k-space and can thus contain low-frequency as well

[1]This approach is different from the commonly used golden-*angle* sampling used in radial sampling.

as high-frequency information. Also, in static MRI, several methods exploiting training signals have been proposed: in [35]–[37], a distribution from which random samples are drawn is constructed, and in [38]–[40], a single image is used at a time to determine the row that is used for sampling. However, to the best of our knowledge, none of these methods have been extended to dynamic MRI.

C. Our contributions

In this paper, we extend the *learning-based framework* of Gözcü et al. [27] for efficiently designing sampling masks based on empirical risk minimization. We preserve the benefits of this recent approach against the state-of-the-art mask design methods, as we do not set any assumptions on the structure of signal, but consider the samples to come from an unknown probability distribution. Both methods are tailored to the anatomy and the reconstruction algorithm at hand, allow direct optimization for a given performance measure and are highly parallelizable. Our scalable version extends this previous work in the following ways leftmargin=*

- We propose a scalable version of the greedy algorithm of [27], which achieves similar reconstruction accuracy by using up to 60 times less resources. This is achieved by implementing a stochastic greedy method.
- This enables a successful extension of this framework to dynamic MRI, where the approach of Gözcü et al. is not computationally feasible.
- Our algorithm allows for keeping the number of samples per frame to be constant, in order for the effective acceleration in scan time to be the consistent with the undersampling rate. This design constraint does not add any computational burden and results from the flexibility of this framework.
- We empirically show the improvement of our method over the state-of-the-art mask designs and several model-based reconstruction algorithms on *in vivo* datasets.
- Finally, given a fixed computational budget, we provide a thorough comparison between our data-driven approach and the model-based approach of tuning parameters of *a priori* assumed distribution to optimize reconstruction quality. We show that our model-free method consistently outperforms this state-of-the-art approach.

III. Learning-based Framework

A. Summary of the learning-based framework

Our work follows the learning-based framework of [27], and we summarize their main ideas hereafter.

We assume that we have a set of training samples $\mathbf{x}_1, \dots, \mathbf{x}_m \in \mathbb{C}^{N\times N\times T}$ representative of an unknown signal of interest $\mathbf{x}$. This means that they are all drawn from the same unknown probability distribution P.

We wish to find the sampling pattern Ω^* that will perform best on $\mathbf{x}$, according to some *performance metric* $\eta_\Omega(\mathbf{x}, \hat{\mathbf{x}})$, and given some constraints on the design of the mask. A performance metric enables quantification of the similarity of a reconstructed image to the ground truth, and common metrics include Peak Signal-to-Noise Ratio (PSNR), Mean Square Error (MSE) or Structural Similarity Index Measure (SSIM) [41]. Regarding the constraints on Ω, it is desirable to restrict the sampling pattern to contain for instance only horizontal and/or vertical phase encoding directions. To formalise this, we define a set $\mathcal{S}$ of subsets of $\{1, \dots, p\}$ which typically contains sets of phase encodes in the k-space. The final mask then takes the form

$$\Omega = \bigcup_{j=1}^{\ell} S_j, \quad S_j \in \mathcal{S} \tag{4}$$

for some $\ell > 0$. We assume that there exists a *cost function* $c(\Omega) > 0$ associated with each sampling pattern, and that the final cost must satisfy

$$c(\Omega) \leq \Gamma \tag{5}$$

for some $\Gamma > 0$, and we consider here the case where the cost is the total number of indices in Ω (constraint on the sampling rate). This then leads to the problem of finding the mask that maximizes

$$\Omega^* = \arg\max_{\Omega\in\mathcal{A}} \mathbb{E}_P\left[\eta_\Omega(\mathbf{x}, \hat{\mathbf{x}})\right] \tag{6}$$

where $\mathcal{A}$ is the set of feasible Ω according to $\mathcal{S}$, $c(\cdot)$, Γ. Due to the problem (6) not being tractable in practice, we look for an approximate maximizer in the form of the *empirical average*, which yields the selection rule that will be used in the sequel

$$\hat{\Omega} = \operatorname*{argmax}_{\Omega\in\mathcal{A}} \frac{1}{m}\sum_{j=1}^{m} \eta_\Omega(\mathbf{x}_j, \hat{\mathbf{x}}_\mathbf{j}). \tag{7}$$

Given that enough training samples are considered, statistical learning theory guarantees that the result obtained using the empirical average will be close to the true average, and Proposition 1 of [27], which formalizes and proves this, extends to the present case as well.

B. Greedy algorithm

Before moving on to our stochastic greedy method, we describe the straightforward application of Gözcü's framework to dMRI. Because finding the exact maximizer of (7) is difficult in general, the greedy algorithm proposed by Gözcü et al. [27] finds an approximate solution by exploiting the fact that the generalization bound dictates that a mask with improved performance should always be favored. This greedy approach has the advantage over state-of-the-art methods of being parameter free in the sense that no tuning is required for the mask selection process, once the reconstruction algorithm and its parameters are given.

The details are specified in Algorithm 1. We start from a base mask Ω, and at each iteration, we create candidate masks $\Omega' = \Omega \cup S$ with each subset $S \in \mathcal{S}$ not yet included in the mask Ω. After reconstructing the image $\hat{\mathbf{x}}$ in the training dataset using the decoder g for all the Ω', the subset S that yields the larger increase regarding the performance metric η is permanently added to the mask Ω. The algorithm continues to add subsets from $\mathcal{S}$ while the cost constraint Γ is not violated.

The algorithm also exhibits a useful *nestedness* property, which means that both the order in which the samples are

Algorithm 1 Greedy mask optimization for dMRI

Input: Training data $\mathbf{x}_1, \dots, \mathbf{x}_m$, reconstruction rule g, sampling subset $\mathcal{S}$, cost function c, maximum cost Γ
Output: Sampling pattern Ω

while $c(\Omega) \leq \Gamma$ **do**
  for $S \in \mathcal{S}$ such that $c(\Omega \cup S) \leq \Gamma$ **do**
    $\Omega' = \Omega \cup S$
    For each j, set $\mathbf{b}_j \leftarrow \mathbf{P}_{\Omega'}\mathbf{\Psi}\mathbf{x}_j$, $\hat{\mathbf{x}}_j \leftarrow g(\Omega', \mathbf{b}_j)$
    $\eta(\Omega') \leftarrow \frac{1}{m}\sum_{j=1}^{m} \eta(\mathbf{x}_j, \hat{\mathbf{x}}_j)$
  $\Omega \leftarrow \Omega \cup S^*$, where

$$S^* = \underset{S: c(\Omega \cup S) \leq \Gamma}{\operatorname{argmax}} \frac{\eta(\Omega \cup S) - \eta(\Omega)}{c(\Omega \cup S) - c(\Omega)}$$

return Ω

added to the mask and their cost are known. Once a given cost is reached (e.g. 30% sampling), all the masks for smaller costs remain available (e.g. the mask for 20% sampling rate).

However, there is a limited applicability of Algorithm 1 to dMRI that comes from the fact that the number of samples increases linearly with the number of frames, and that the reconstruction algorithms are generally more expensive to run than in the static case. This makes the overall running time of Algorithm 1 impractical for the present case, as we will see in Section IV.

C. Stochastic greedy algorithm

Our main contribution is the scalable version of Algorithm 1, which makes it suited to problems such as dMRI. Instead of considering the whole set of samples $\mathcal{S}$, we select a subset $\mathcal{S}^{'} \subseteq \mathcal{S}$ either at random (Algo. 2), or at random *from a given frame*, which will be denoted as $\mathcal{S}_t^{'}$ (Algo. 3). Then, the same greedy procedure as Algorithm 1 is run, and at the end of an iteration, either a new subset of $\mathcal{S}$ is selected at random (Algo. 2), or the index of the selected frame is incremented (Algo. 3) and a subset is drawn at random from this frame. The number of samples used at each iteration is given by the batch size k. It is important to highlight that this approach preserves all the benefits of the previous greedy approach: our method remains nearly parameter free even when considering the batch size k. Empirical results in section IV-D suggest that the tuning of this parameter is simple and does not change the accuracy of reconstruction when chosen as a reasonable fraction of the total number of phase encoding lines.

Algorithm 2 Stochastic greedy mask optimization for dMRI

Input: Training data $\mathbf{x}_1, \dots, \mathbf{x}_m$, reconstruction rule g, sampling subset $\mathcal{S}$, cost function c, max. cost Γ, batch size k
Output: Sampling pattern Ω

while $c(\Omega) \leq \Gamma$ **do**
  Pick $\mathcal{S}^{'} \subseteq \mathcal{S}$, at random, with $|\mathcal{S}^{'}| = k$
  for $S \in \mathcal{S}^{'}$ such that $c(\Omega \cup S) \leq \Gamma$ **do**
    Follow steps 3 - 6 of Algorithm 1
return Ω

The main difference between Algorithms 2 and 3 lies in the way the random subset is chosen. This difference has the practical implication that the sampling masks designed in Algorithm 3 will have the same number of samples per frame, which is desirable for a dMRI scan [25], as undersampling frames at different rates may alter the temporal resolution, thus leading to potentially missing critical temporal events.

Algorithm 3 Stochastic cycling greedy mask optimization for dMRI

Input: Training data $\mathbf{x}_1, \dots, \mathbf{x}_m$, reconstruction rule g, sampling subset $\mathcal{S}$, cost function c, max. cost Γ, batch size k
Output: Sampling pattern Ω

$t = 1$
while $c(\Omega) \leq \Gamma$ **do**
  Pick $\mathcal{S}_t^{'} \subseteq \mathcal{S}_t$, at random, with $|\mathcal{S}_t^{'}| = k$
  for $S \in \mathcal{S}_t^{'}$ such that $c(\Omega \cup S) \leq \Gamma$ **do**
    Follow the steps 3 - 6 of Algorithm 1
  $t = t \bmod n_{\text{frames}} + 1$
return Ω

D. Learning-based variable density

An intuitive approach given in [27] is to find an approximative solution to the combinatorial problem (7) by generating a set of candidate masks $\Omega_1, \dots, \Omega_L$ using parametric variable-density methods, and choose the one with the best empirical performance on the training set (Algorithm 1). While similar ideas have already been used when performing parameter sweeps in existing works (e.g., see [35]), the framework of [27] justifies why the empirical performance is the correct quantity to optimize.

Algorithm 4 Learning-based variable density (LB-VD)

Input: Training data $\mathbf{x}_1, \dots, \mathbf{x}_m$, reconstruction rule g, candidate masks $\Omega_1, \dots, \Omega_L$
Output: Sampling pattern Ω

for $\ell = 1, \dots, L$ **do**
  For each j, set $\mathbf{b}_j \leftarrow \mathbf{P}_{\Omega_\ell}\mathbf{\Psi}\mathbf{x}_j$, $\hat{\mathbf{x}}_j \leftarrow g(\Omega_\ell, \mathbf{b}_j)$
  $\eta_\ell \leftarrow \frac{1}{m}\sum_{j=1}^{m} \eta(\mathbf{x}_j, \hat{\mathbf{x}}_j)$
$\Omega \leftarrow \Omega_{\ell^*}$, where $\ell^* = \operatorname{argmax}_{\ell=1,\dots,L} \eta_\ell$
return Ω

E. Noisy setup

In the noisy case, we again consider the same setup as in [27], where we do not have access to the exact training samples $\mathbf{x}_1, \dots, \mathbf{x}_m$, but only to a noisy version of those

$$\mathbf{z}_j = \mathbf{x}_j + \mathbf{v}_j, \ j = 1, \dots, m \tag{8}$$

where $\mathbf{v}_j$ is the noise in the samples, and we have the relation $\mathbf{w}_j = \mathbf{\Psi}\mathbf{v}_j$. Again, as we want to learn the true underlying signal and not the noisy one, we use a denoiser $\xi(\mathbf{z}_j) = \mathbf{x}_j + \tilde{\mathbf{v}}_\mathbf{j}$ that reduces the noise level, i.e. $\mathbb{E}[\|\tilde{\mathbf{v}}_\mathbf{j}\|] \leq \mathbb{E}[\|\mathbf{v}_j\|]$, and the empirical risk minimization formulation is then adapted to

$$\hat{\Omega} = \underset{\Omega \in \mathcal{A}}{\operatorname{argmax}} \frac{1}{m}\sum_{j=1}^{m} \eta_\Omega(\mathbf{x}_j + \tilde{\mathbf{v}}_\mathbf{j}, \hat{\mathbf{x}}(\mathbf{P}_\Omega\mathbf{\Psi}(\mathbf{x}_j + \mathbf{v}_j)). \tag{9}$$

Using the noisy training signal in the choice of $\mathbf{b}$ from equation (1) allows the algorithm to choose samples that will enable it to denoise the testing signal, which also has noisy samples. The generalization bound of Proposition 2 of [27] remains valid in the present case.

IV. Numerical Experiments

A. Implementation details

Reconstruction algorithms: As detailed in the Section II-A, we consider three reconstruction algorithms, namely *k-t FOCUSS* (KTF) [6], *Iterative Soft-Thresholding* (IST) [12] and *ALOHA* [21]. Their parameters were selected to maintain a good empirical performance across all sampling rates considered.

leftmargin=*

- For *KTF*, we used 2 outer iterations with 40 inner iterations, and a low-phase estimate of $\mathbf{W}$ with 4 phase encodes and set the power in the diagonal of $\mathbf{W}$ to $p = 0.5$, and the Lagrangian parameter of the inner problem to $\lambda = 0$.
- For *IST*, the regularization parameter was set to $\lambda = 0.046$ and decreased by 1.7% at each iteration, as suggested in [12]. The maximal number of iterations was 100.
- Finally, for *ALOHA*, the annihilating filter was of size 5×5, with three levels of pyramidal decomposition with tolerances $(10^{-1}, 10^{-2}, 10^{-3})$ at each scale. The ADMM parameter was set to $\mu = 10$.

Mask selection methods: In addition to the greedy methods in Algorithms 1, 2, and 3, we consider additional comparison baselines from the literature: leftmargin=*

- *Coherence-VD* [23]: We consider a random *variable-density* sampling mask with Gaussian density and a fixed number of fully sampled low frequency phase encodes. We varied the standard deviation of the Gaussian distribution to minimize the coherence using a Monte-Carlo procedure, as suggested in [13], [23].
- *LB-VD* (Algorithm 4): We considered a random *variable-density* sampling mask with Gaussian density sampling. In this setting, we optimized the number of fully sampled low frequency phase encodes, as well as the standard deviation of the Gaussian distribution in order to maximize the performance metric on the same training set that was used for the greedy algorithm. This was achieved using a parameter sweep, and for each set of parameters, the results were averaged over 20 random masks produced by sampling from the corresponding distribution.
- *Golden-ratio Cartesian sampling* [26]: This method, referred to as *golden*, does not have free parameters. It a nonlinear function of the golden-ratio to distribute the phase encodes across the frames.

The VISTA [25] approach is also a parametric method, and we observed that it yields highly similar results to that of Gaussian variable-density sampling, so we prefer not to report VISTA results for brevity.

The nomenclature for the different reconstruction and sampling algorithms used in the sequel is summarized in Table I.

Data sets: The first data set was acquired in seven healthy adult volunteers with a balanced steady-state free precession (bSSFP) pulse sequence on a whole-body Siemens 3T scanner using a 34-element matrix coil array. Several short-axis cine images were acquired during a breath-hold scan. Fully sampled Cartesian data were acquired using a 256×256 grid, with relevant imaging parameters including $320\,\mathrm{mm} \times 320\,\mathrm{mm}$ field of view (FoV), $6\,\mathrm{mm}$ slice thickness, $1.37\,\mathrm{mm} \times 1.37\,\mathrm{mm}$ spatial resolution, $42.38\,\mathrm{ms}$ temporal resolution, $1.63/3.26\,\mathrm{ms}$ TE/TR, 36° flip angle, $1395\,\mathrm{Hz/px}$ readout bandwidth. There were 13 phase encodes acquired for a frame during one heartbeat, for a total of 25 frames after the scan.

Table I
Nomenclature for the algorithms used throughout this work, with each algorithm and its corresponding abbreviation.

Reconstruction Algorithms	k-t FOCUSS [6]	*KTF*
	Iterative Soft-Thresholding [12]	*IST*
	Annihilating filter-based low-rank Hankel matrix [21]	*ALOHA*
Sampling Optimization Algorithms	Coherence-based Gaussian variable-density random sampling [23]	*Coherence-VD*
	Learning-based Gaussian variable-density sampling (Algorithm 4)	*LB-VD*
	Golden-ratio Cartesian sampling [26]	*Golden*
	Learning-based greedy algorithm (Algorithms 1 to 3)	*Greedy*

The Cartesian cardiac scans were then combined to single coil data from the initial $256 \times 256 \times 25 \times 34$ size, using adaptive coil combination [42], [43], which keeps the image complex. This single coil image was then cropped to a $152 \times 152 \times 17$ image. This is done because a large portion of the periphery of the images are static or void, and also to enable a greater computational efficiency. These scans are the ones we used as the basis of the subsequent numerical experiments.

The other data set that we used comprised 4 vocal tract scans with a 2D HASTE sequence (T2 weighted single-shot turbo spin-echo) on a 3T Siemens Tim Trio using a 4-channel body matrix coil array. Fully sampled Cartesian data were acquired using a 256×256 grid, with $256\,\mathrm{mm} \times 256\,\mathrm{mm}$ field of view (FoV), $5\,\mathrm{mm}$ slice thickness, $1\,\mathrm{mm} \times 1\,\mathrm{mm}$ spatial resolution, $98/1000\,\mathrm{ms}$ TE/TR, 150° flip angle, $391\,\mathrm{Hz/px}$ readout bandwidth, $5.44\,\mathrm{ms}$ echo spacing (256 turbo factor). There was a total of 10 frames acquired, which were recombined to single coil data using adaptive coil combination as well [42], [43].

Performance metrics: Throughout our comparison, we use Peak Signal-to-Noise Ratio (PSNR) as the standard performance metric, as well as structural similarity (SSIM) [41], which was applied to dMRI by Otazo et al. in [15].

Greedy setup: In the experiments to follow, we will typically consider the sampling subset $\mathcal{S}$ to be the set of phase encode lines across all frames (i.e. for an image of size $152 \times 152 \times 17$, the full set will contain $|\mathcal{S}| = 152 \times 17 = 2584$ sets of subsets). Then, the cost function c will be the sampling rate of the mask, and Γ will be 30% sampling. The performance metric η will either be PSNR or SSIM.

B. Computational costs

Greedy algorithms 1 to 3: The implementation of the greedy algorithms was done using MATLAB, and the simulation were run on a cluster using its Parallel Computing Toolbox. The reconstruction times for the different settings

Table II
RUNNING TIME OF THE GREEDY ALGORITHMS FOR DIFFERENT DECODERS AND TRAINING DATA SIZES. THE SETTING CORRESPONDS TO n_x, n_y, n_{FRAMES}, n_{TRAIN}. n_{PROCS} IS THE NUMBER OF PARALLEL PROCESSES USED BY EACH SIMULATION. * MEANS THAT THE RUNTIME WAS EXTRAPOLATED FROM A FEW ITERATIONS.

Algorithm	Setting	Greedy [27]			Stochastic Greedy			Speedup
		Time	n_{procs}	n_{recon}	Time	n_{procs}	n_{recon}	
KTF	152×152×17×3	6d 23h	152	$5.1 \cdot 10^6$	11h 40	38	$8.8 \cdot 10^4$	58
	256×256×10×2	$\sim$ 7d 8h*	256	$3.3 \cdot 10^6$	12h 20	64	$9.8 \cdot 10^4$	57
IST	152×152×17×3	3d 11h	152	$5.1 \cdot 10^6$	5h 30	38	$8.8 \cdot 10^4$	60
ALOHA	152×152×17×3	$\sim$ 25d 1h*	152	$5.1 \cdot 10^6$	1d 14h 25	38	$8.8 \cdot 10^4$	62

(image sizes, number of training samples) are displayed in the Table II. First of all, note that the overall runtime heavily depends on the reconstruction algorithm in use, and varies from 3.5s for KTF and 1.2s for IST to 73.5s for ALOHA; however this does not take into account the *significant* latency introduced by running the simulation in parallel. Due to the very small number of samples used by the stochastic algorithm, the running time improvement over the standard greedy algorithm is tremendous. We will see in Section IV-C that there is *nearly no performance loss* linked to this acceleration.

It is also important to highlight that these computations are carried out *offline*, and have to be done only once for a fixed anatomy and resolution, while giving access to the masks up to the highest sampling rate achieved (typically 30% in the present case) due to the nestedness property of the greedy algorithm. Given the improvements to both the running time and the scalability of our algorithm compared to the previous version of the greedy algorithm, as well as the result of yielding a mask tailored for a certain anatomy, the longer computational time should not be seen as a critical issue.

Coherence-based variable-density Gaussian sampling (Coherence-VD): The computation times using variable-density methods are almost negligible compared to the greedy running time: tuning the mask for each sampling rate considered does not involve any reconstruction, so the process is very fast and will not be reported.

Learning-based variable-density Gaussian sampling (LB-VD - Algorithm 4): In this setting, we optimize the parametric Gaussian distribution for PSNR and we summarize the parameters that we examined in Table III. The parameters that we considered are the standard deviation of the distribution, as well as the size of the fully sampled low-frequency region. For each set of parameters and training samples, the results were averaged across 20 draws. The number of reconstructions is similar to the ones performed by the stochastic greedy algorithms, but the running time is much shorter. This is due to the fact that this problem can be distributed more efficiently and requires much less communication between workers than the greedy algorithms. This model-based method will be compared with the greedy methods in the sequel.

A first downside appears in the fact that while the LB-VD mask optimization requires roughly the same number of reconstructions as the stochastic greedy method, it only provides masks for a discrete set of sampling rates (in our comparisons, we used 12 sampling rates from 2.5% to 30%, with 2.5% intervals). However, the greedy method enables mask optimization for a continuous range of sampling rates by exploiting the information from other sampling rates to further guide the mask design which is not the case for LB-VD.

Table III
COMPARISON OF THE LEARNING-BASED RANDOM VARIABLE-DENSITY GAUSSIAN SAMPLING OPTIMIZATION (ALG. 4) FOR DIFFERENT SETTINGS. n_{PARS} DENOTES THE NUMBER OF PARAMETERS THAT WERE TUNED. FOR EACH SET OF PARAMETERS, THE RESULTS WERE AVERAGED ON 20 MASKS DRAWN AT RANDOM FROM THE DISTRIBUTION CONSIDERED. THE COMPUTATIONS WERE DONE FOR 12 DIFFERENT SAMPLING RATES.

Algo.	Setting	n_{pars}	n_{recon}	n_{procs}	Time
KTF	152×152×17×3	120	$8.6 \cdot 10^4$	38	6h 30
	256×256×10×2*	240	$1.05 \cdot 10^5$	64	6h 45
IST	152×152×17×3	120	$8.6 \cdot 10^4$	38	3h 20
ALOHA	152×152×17×3	120	$8.6 \cdot 10^4$	38	1d 8h

C. Comparison between the greedy algorithms

In this first experiment, we compare the three variations of the greedy algorithms that were previously discussed, namely the regular *greedy* algorithm 1 the *stochastic* greedy algorithm 2 which takes k samples (entire lines in Fourier space at different phase encodes) uniformly at random at each iteration, and the *stochastic cycling* greedy algorithm 3, which takes k samples in a given frame at each iteration. We use the cardiac dataset and split the data between 3 training and 4 testing samples. We chose the number of stochastic samples to be $k = 38$, as Figure 1 highlights that the PSNR is very close for all three greedy methods, and nearly equal in the IST case. This fact can be surprising considering that the *stochastic* and *stochastic cycling* methods use 68 times less samples than the *greedy* algorithm at each iteration. A similar behavior was observed for larger k, and generally, unless one uses extremely small batches of samples (e.g. 20 or less), the stochastic greedy algorithms will yield the same results as the regular *greedy* algorithm. The effect of batch size will be more thoroughly discussed in the next section. Note that ALOHA was not run in this setup due to the prohibitive runtime of the regular greedy algorithm on it.

Visually speaking, on Figure 2, the reconstruction are as well very close across all three algorithms and for both sampling rates, yet the masks are slightly different. We must remember that as we are seeking an approximate maximizer, several sampling patterns will satisfy this criterion, as those result show that achieving a similar reconstruction accuracy does not mean that the masks will be close. Moreover, we

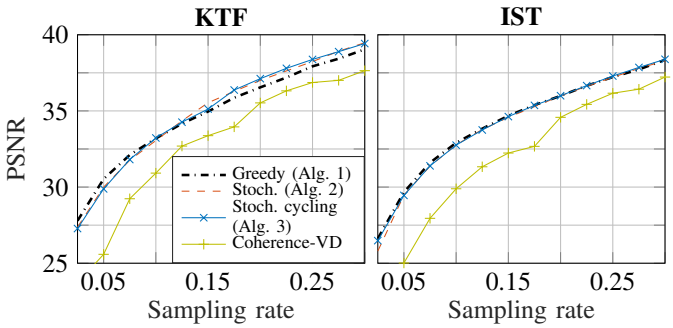

Figure 1. PSNR as a function of sampling rates for the three greedy algorithms considered, comparing the learning-based *greedy* result with the Coherence-VD sampling [23] for both k-t FOCUSS (left) and Iterative Soft-Thresholding (right). The stochastic and stochastic cycling used batches of 38 elements, and the results were averaged on 4 testing data of size 152×152×17.

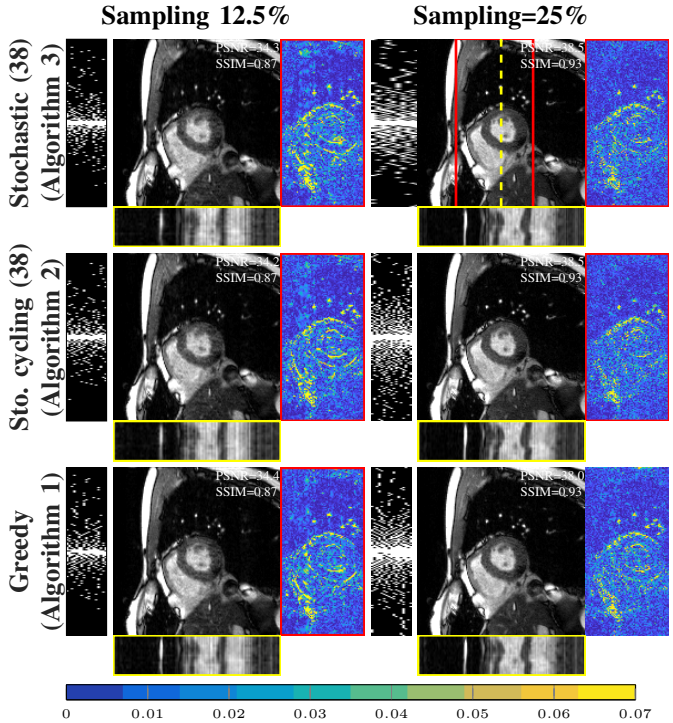

Figure 2. Comparison between the different forms of greedy algorithms using k-t FOCUSS as a reconstruction methods, for two different sampling rates (12.5% and 25%), using a batch size of 38 on an image of size 152×152×17. The ninth frame is displayed, and the temporal profile is taken across the vertical line shown on the top right image.

see that the the stochastic algorithms actually outperforms the *greedy* algorithm in the range $20-30\%$ with k-t FOCUSS. This can be viewed as the randomness allowing to explore a greater richness of mask designs by helping to exit the local optima in which the greedy method could get stuck.

Overall, as the three algorithms yield similar PSNR and visual quality, we will use the *stochastic cycling* algorithm, as it has the best performance with the additional benefit of imposing a fixed number of samples per frame. In the sequel, this algorithm will use a batch of 38 samples with training data of size 152×152×17×3, unless specified otherwise.

D. Influence of the batch size k on the mask design

In this experiment, we ran the greedy algorithms with different batch sizes in the same settings as in the numerical experiment described in Section IV-C. Figure 3 displays the PSNR of the reconstructions for the *stochastic* and the

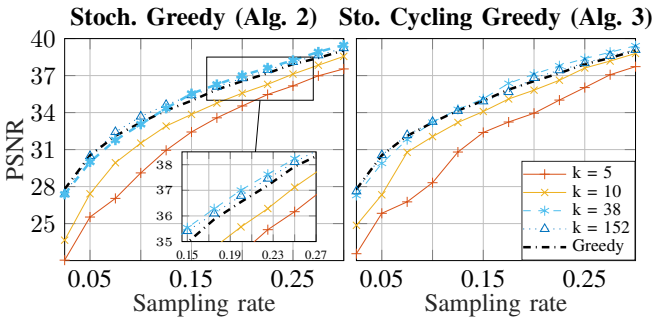

Figure 3. PSNR as a function of the sampling rate for k-t FOCUSS, comparing the effect of the batch size on the quality of the reconstruction for Algorithms 2 (on the left) and 3 (on the right). The result is averaged on 4 testing images of size 152 × 152 × 17. Here, *Greedy* corresponds to the standard greedy algorithm of [27] adapted to dMRI, and is shown for comparison.

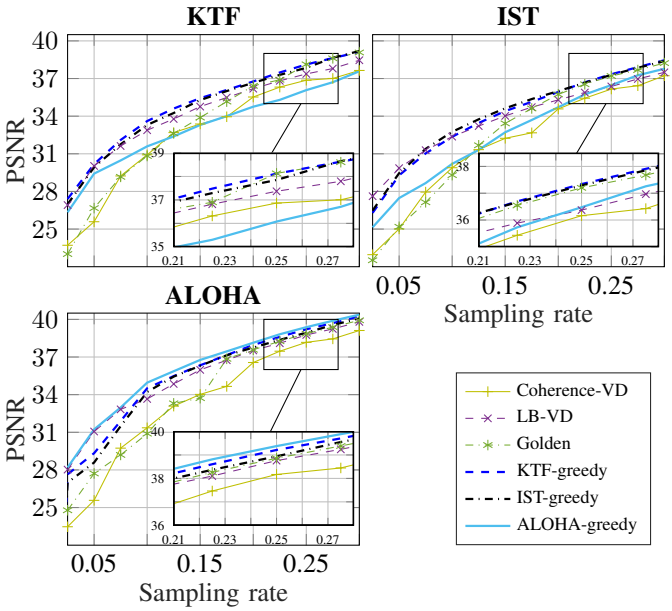

Figure 4. PSNR as a function of sampling rate for the three reconstruction algorithms considered, comparing the learning-based *greedy* result with the *coherence-based* Gaussian sampling [23], *Learning-based variable-density* (Algorithm 4 - optimized for each reconstruction algorithm), and *golden* angle Cartesian sampling [26], averaged on 4 testing images of size 152×152×17.

stochastic cycling greedy algorithms respectively. We only considered k-t FOCUSS for brevity (Figures 13 and 14 in the appendix show the designed masks for varying batch sizes). The same trend is observed on both plots, where very small batch sizes yield suboptimal results, and PSNR performance of the standard greedy sampling is reached with as few as 38 samples (roughly 1.5% of all possible samples). Unless the batch size is extremely small, the results suggest that the masks obtained with Algorithms 2 and 3 yield satisfactory reconstruction quality, i.e. the similar or higher quality than the standard greedy algorithm.

E. Comparison to baselines

The comparison to baselines is shown on Figures 4 and 5, where we see that the learning-based method yields masks which consistently improve the results compared to all variable-density methods used. Even though some variable-density techniques are able to provide good results for some sampling rates and algorithms, our learning-based technique

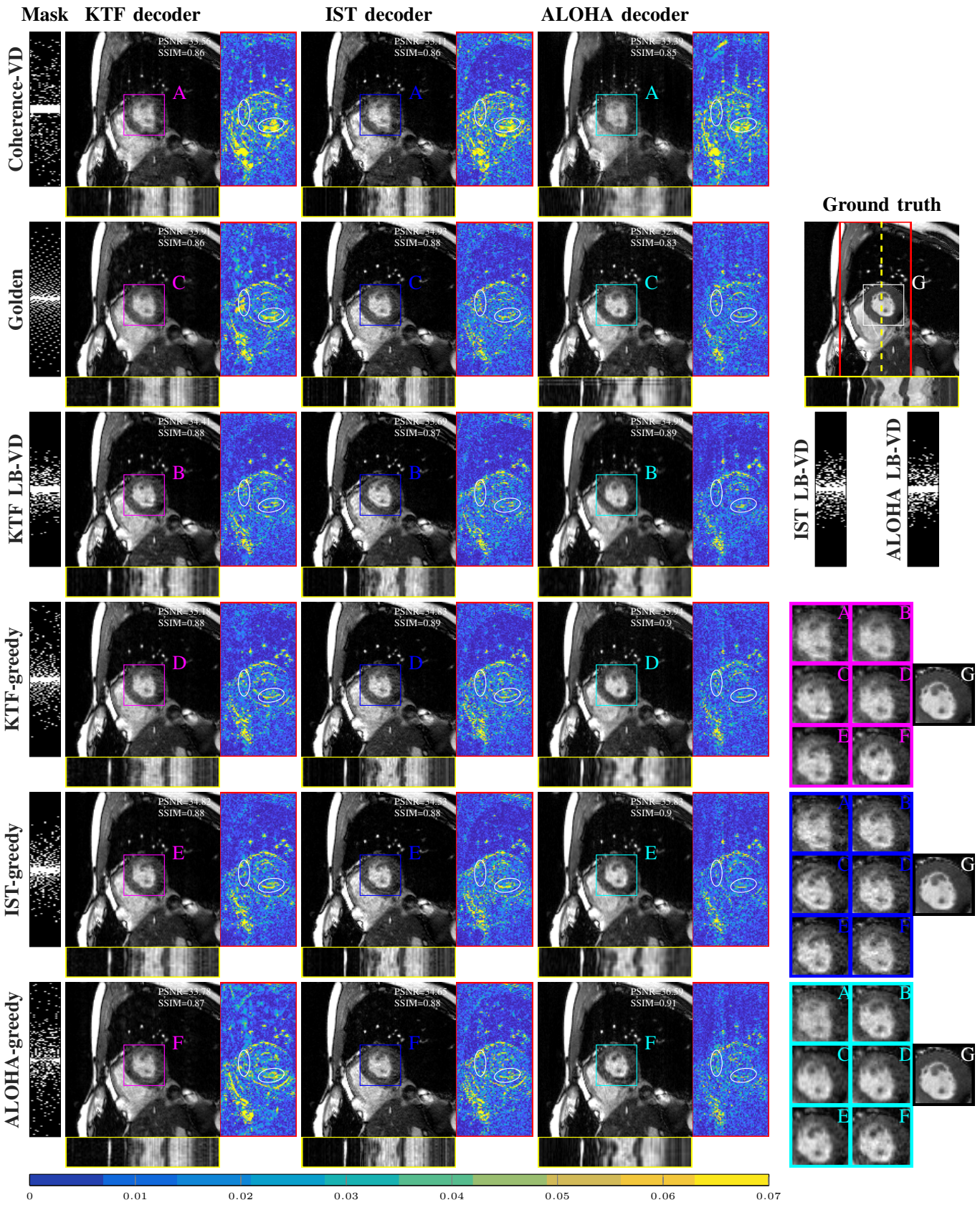

Figure 5. Comparison of the different reconstruction masks and decoders, for a sampling rate of 15% on a single sample with its PSNR/SSIM performances. The comparison are the *Gaussian* sampling [23], *Learning-based variable-density* (Algorithm 4 - optimized for each reconstruction algorithm), and *golden* angle Cartesian sampling [26], as well as the masks optimized for k-t FOCUSS [6], Iterative Soft-Thresholding [12], and ALOHA [21] using *greedy algorithm*. These are images of size 152×152×17. The ninth frame is displayed, and the temporal profile is taken across the vertical line shown on the ground truth, and is displayed below each image. Next to each image the error map is shown. It is computed with respect to a normalized ground truth and corresponds to the region between the vertical red lines on the ground truth. On the bottom right of the image, a zoom onto the region of interest is presented. An additional comparison of LB-VD and Greedy is available in Figure 15 in the appendix.

is able to consistently provide improvement over this state-of-the-art. Compared to Coherence-VD, there is always at least 1 dB improvement at any sampling rate, and it can be as much as 6.7 dB at 5% sampling rate for ALOHA. For *golden*, there is an improvement larger than 1.5 dB prior to 15% rate, and around 0.5dB after for all decoders. Figure 4 also clearly indicates that the benefits of our learning-based framework become more apparent towards higher sampling rates, where the performance improvement over LB-VD reaches up to 1 dB. Towards lower sampling rates, with much fewer degrees of freedom for mask design, the greedy method and LB-VD yield similar performance as expected. As shown in Figure 5, the learning-based masks tend to conserve better the sharp contrast transition compared to the variable-density techniques.

F. Cross-performances of reconstruction algorithms

Referring again to Figures 4 and 5, there are several observations to be made regarding the masks resulting from the greedy procedure across the decoders. First of all, the masks for k-t FOCUSS and IST yield performances that are very close, even when pairing them to the other decoder, where only a small drop of less than 0.5 dB is observed. Paired with the ALOHA decoder, any of these masks outperforms the baselines at the majority of the sampling rates considered.

The mask trained with ALOHA yields performs suboptimally on k-t FOCUSS and IST, yet remaining in competition with the coherence-based mask. This suggests that even though there is a large influence of the decoder over the design of the mask, the mask still successfully captures some structure inherent to the dataset used, allowing for generalizable performances even when the mask is not paired with the decoder for which it was trained. However, pairing both yields superior results.

Additionally, we notice on Figure 5 that comparing the reconstruction algorithms with variable-density-based methods do not allow for a faithful performance comparison of the reconstruction algorithms: the performance is very close for each reconstruction algorithm. Whereas considering the reconstruction algorithm jointly with a sampling pattern optimized with a model-free approach makes the performance difference much more clear: ALOHA with its corresponding mask clearly outperforms KTF and IST, which was not clear by looking only at reconstruction with VD-based masks. This is further discussed in Appendix B where we compare the cross-performance of LB-VD and greedy masks in greater detail.

G. Cross-performances of performance measures

Up to here, we used PSNR as the performance measure, and we now compare it with the results of the greedy algorithm paired with SSIM, a metric that more closely reflect perceptual similarity. For brevity, we only consider ALOHA in this section. In the case where we optimized for SSIM, we noticed that unless a low-frequency initial mask is given, the reconstruction quality would mostly stagnate. This is why we chose to start the greedy algorithm with 4 low-frequency phase encodes at each frame in the SSIM case.

The reconstructions for PSNR and SSIM are shown on Figure 6, where we see that the learning-based masks outperform

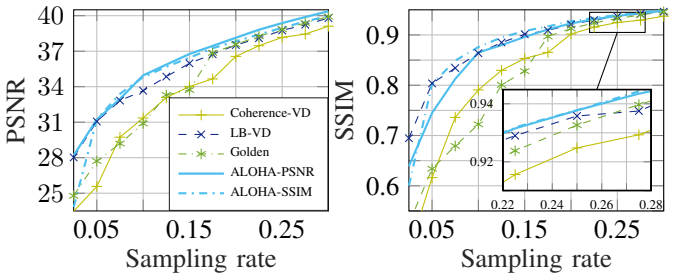

Figure 6. PSNR and SSIM as a function of sampling rate for ALOHA, comparing the learning-based *greedy* results optimized for PSNR and SSIM with the three baselines, averaged on 4 testing images of size 152×152×17.

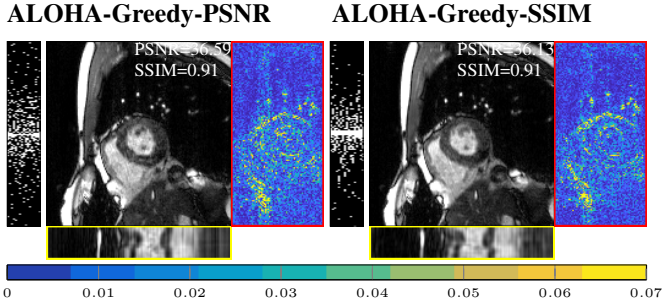

Figure 7. Comparison of the sampling masks optimized for PSNR and SSIM with ALOHA, at 15% sampling. The images and masks can be compared to those of Figure 5, as the settings are the same.

the state-of-the-art across all sampling rates except at 2.5% in the SSIM case. The quality of the results is very close for both masks, but each tends to perform slightly better with the performance metric for which it was trained. The fact that the ALOHA-SSIM result at 2.5% has a very low SSIM is due to the fact that we impose 4 phase encodes across all frames, and the resulting sampling mask at 2.5% is a low pass mask in this case.

A visual reconstruction is provided in Figure 7, we see that there is almost no difference in reconstruction quality, and that the masks remain very similar. Overall, we observe in this case that the performance metric selection does not have a dramatic effect on the quality of reconstruction, and our greedy framework is still able to produce masks that outperform state-of-the-art when optimizing SSIM instead of PSNR.

H. Noisy experiments

In order to test the robustness of our framework to noise, we artificially added bivariate circularly symmetry complex random Gaussian noise to the normalized complex images, with a standard deviation $\sigma = 0.05$ for both the real and imaginary components. We then tested to see whether the greedy framework is able to adapt to the level of noise by prescribing a different sampling pattern than in the previous experiments.

We chose to use V-BM4D [44] as denoiser with its default suggested mode using Wiener filtering and low-complexity profile, and provided the algorithm the standard deviation of the noise as the denoising parameter. The comparison between the fully sampled denoised images and the original ones yields an average PSNR of 24.95 dB across the whole dataset. Due to the fact that none of the reconstruction algorithms that we used have a denoising parameter incorporated, we simply apply the V-BM4D respectively to the real and the imaginary parts of

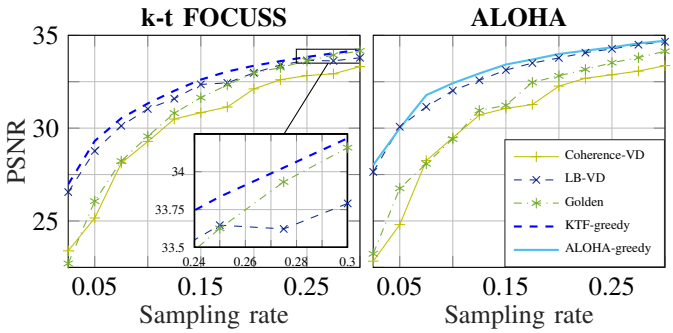

Figure 8. PSNR as a function of sampling rate for both reconstruction algorithms considered, comparing the learning-based *greedy* result with the three baselines, averaged on 4 noisy testing images of size 152×152×17. The PSNR is computed between the denoised reconstructed image and the original (not noisy) ground truth.

the result of the reconstruction. The results that we obtain are presented on the Figures 8 and 9.

It is interesting to notice on Figure 9 that the learning-based framework outperforms the baselines that are not learning-based by a larger margin than in the noiseless case, and this is again especially true at low sampling rates. In this case however, the difference between the greedy and LB-VD methods is much smaller, and this might be explained by the fact that noise corrupts the high frequency samples, and thus the masks concentrate more around low-frequencies, leaving less room for designs that largely differ.

We see a clear adaptation of the resulting learning based mask, as shown by comparing Figures 5 and 9: the masks KTF-greedy and ALOHA-greedy, which are trained on the noisy data, are closer to low-pass masks, due to the high-frequency details being lost to noise, and hence, no very high frequency samples are added to the mask.

Also, notice than even if the discrepancy in PSNR is only around $0.8 - 1$ dB between the golden ratio sampling and the optimized one, the temporal details are much more faithfully preserved by the learning-based approach, which is crucial in dynamic applications. The inadequacy of coherence-based sampling is highlighted in this case, as very little temporal information is captured in the reconstruction with both decoders. Also, for both decoders, there is a clear improvement on the preservation of the temporal profile when using learning-based masks compared to the baselines; the improvement of the ALOHA-greedy mask of around 3dB also shows how well our framework is able to adapt to this noisy situation, whereas Coherence-VD yields results of unacceptable quality.

I. Experiments with larger image size

In these last experiments, we consider both the single coil cardiac dataset as well as the vocal imaging dataset both of size $256 \times 256 \times 10$. The cardiac dataset was trained on 5 samples and tested on 2, using only the first ten frames of each scan, whereas the vocal one used 2 training samples and 2 testing samples. In this setup, the k-space of the cardiac dataset tends to vary more from one sample to another than the vocal one, making the generalization of the mask more complicated. This issue would require more training samples, but imposing the greedy algorithm to start with 4 central phase encoding lines on each frame was found to be sufficient to acquire the peaks

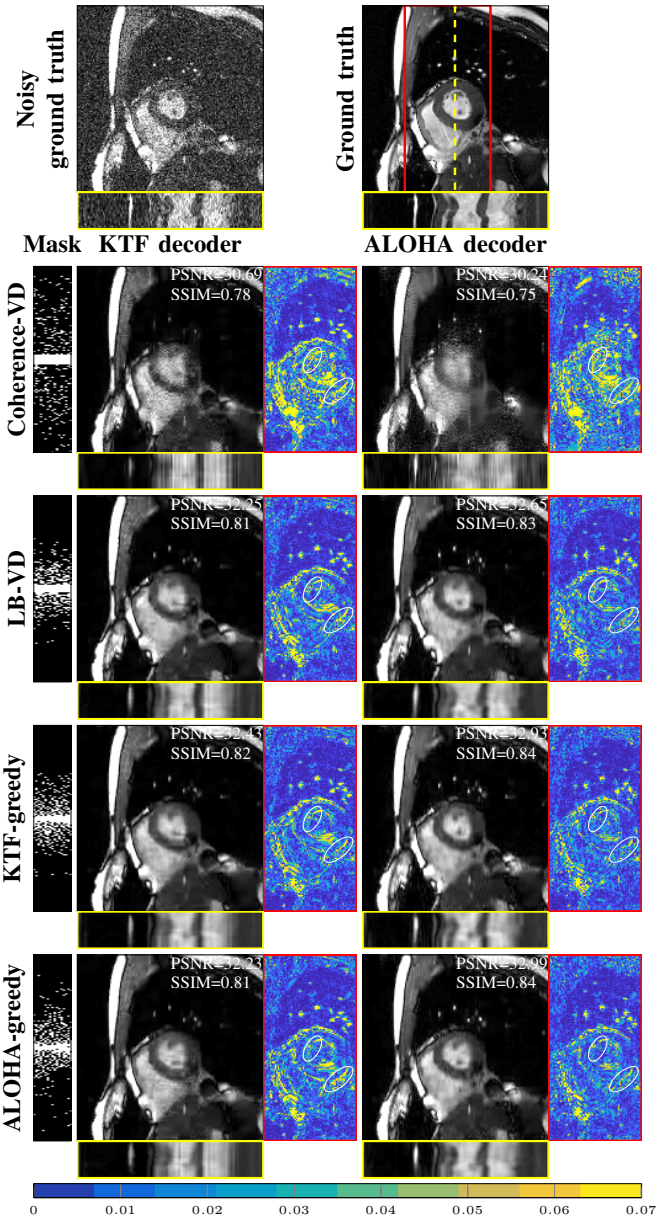

Figure 9. Reconstructed denoised version from the noisy ground truth on the first line, at 15% sampling. The PSNR is computed with respect to the original ground truth on the top right.

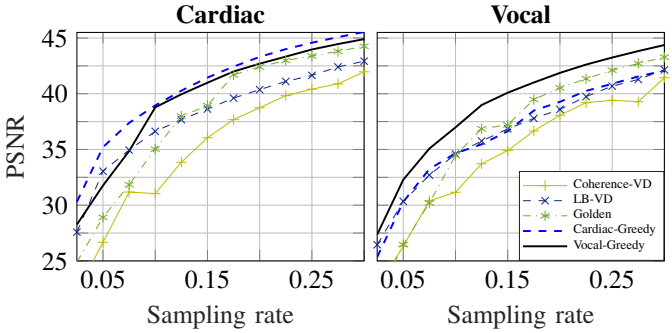

Figure 10. PSNR as a function of sampling rate for KTF, comparing the learning-based *greedy* result with both baselines, averaged on 2 testing images for both cardiac and vocal data sets of size 256×256×10.

in the k-space across the whole dataset. *Cardiac-greedy* refers to the greedy algorithm using cardiac data, and *Vocal-greedy* is its vocal counterpart. The algorithm used a batch of size

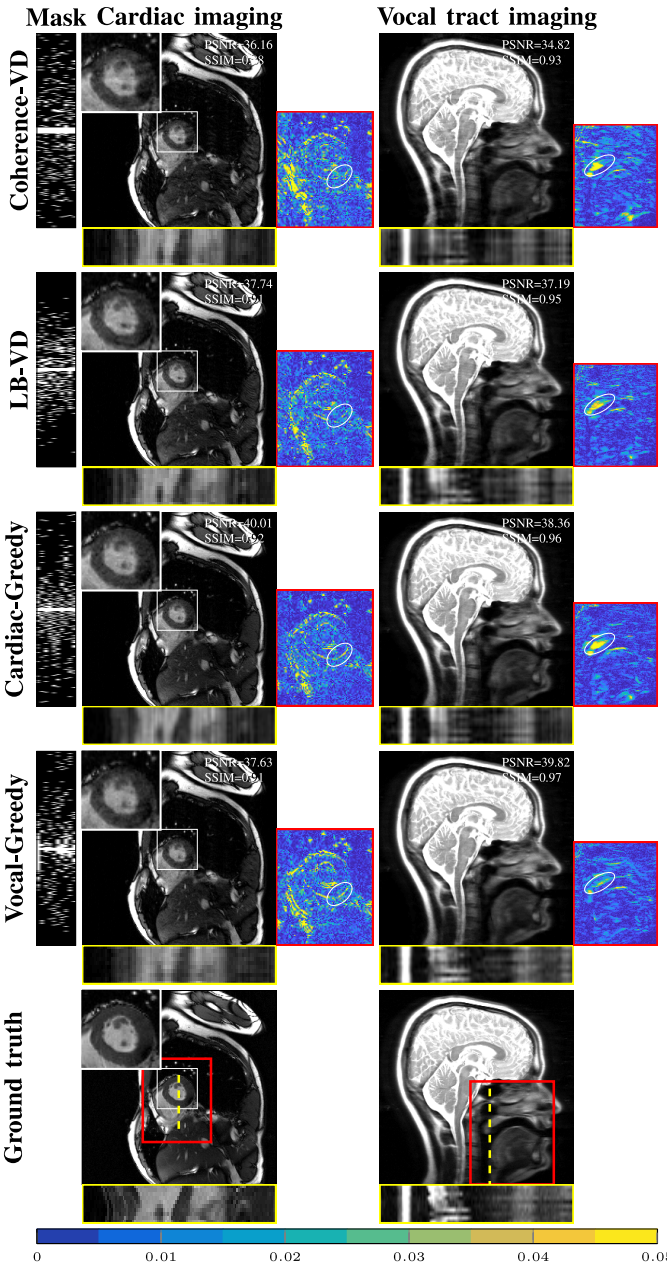

Figure 11. Reconstruction for KTF at 15% sampling for the cardiac and vocal anatomies of size 256×256×10. Figures showing different frames for the vocal and cardiac images are available in Appendix C.

$k = 64$ at each iteration, and the results were obtained using only KTF.

The results are reported on the Figures 10 and 11, and we see that, for the both datasets, the greedy approach provides superior results against state-of-the-art sampling methods across all sampling rates. It is striking that, in this setting, the greedy approach outperforms even more convincingly all the baselines, and the LB-VD approach, in this case, is outperformed by more than 2dB by the greedy approach, where it remained very competitive in the other settings. This difference is clear in the temporal fidelity of both reconstructions on Figure 11, where we see that the LB-VD approach loses sharpness and accuracy compared to the greedy one.

J. Comparison across anatomies

The main complication coming from applying the masks across anatomies is that the form of the k-space might vary heavily across datasets, as shown on the last row of Figure 11: the vocal spectrum is very sharply peaked, while the cardiac one is much broader. Comparing the cross-performances on Figures 11, we see that the and *vocal-greedy* masks generalizes much better on the cardiac datasets than the other way around. This can be explained from the differences in the spectra: the cardiac one being more spread out, the cardiac mask less faithfully captures the very low frequencies of the k-space, which are absolutely crucial to a successful reconstruction on the vocal dataset, thus hindering the reconstruction quality. Also, we see that it is important for the trained mask to be paired with its anatomy to obtain the best performance.

V. Conclusion

We presented a novel method for sampling optimization in the dMRI setting which brings significant image quality improvements over the state-of-the-art methods. These VD-based methods limit the performance of CS applied to MRI through their underlying model and are consistently outperformed by our model-free and adaptive method on different *in vivo* datasets, across several decoders, field of views and resolutions. Our findings highlight that sampling design should not be considered in isolation from data and reconstruction algorithm, as using a mask that is not specifically optimized can considerably degrade the performance of the algorithm.

We also showed that our method largely resolves the scalability issues of [27] by resorting to a stochastic greedy method, while preserving its advantages of being intuitive, versatile, and easy to pair with any reconstruction and anatomy. Reducing the resources used in the greedy algorithm by as much as a 60 times was shown to have no negative impact on the quality of reconstruction achieved within our framework. Moreover, our approach is able to provide masks with performance guarantees on unseen data, whereas the VD approach relies on random sampling and parameter tuning, which complicates the incorporation of compressed sensing-based methods into routine clinical MRI [45]. Finally we anticipate that the proposed framework could also greatly benefit other settings such as 3D (d)MRI and parallel imaging in general.

Acknowledgment

This work has received funding from the European Research Council (ERC) under the European Union's Horizon 2020 research and innovation program (grant agreement n° 725594 - time-data) and from Hasler Foundation Program: Cyber Human Systems (project number 16066).

References

[1] M. Saeed, T. A. Van, R. Krug, S. W. Hetts, and M. W. Wilson, "Cardiac MR imaging: current status and future direction," *Cardiovascular diagnosis and therapy*, vol. 5, no. 4, p. 290, 2015.

[2] E. J. Candes, J. K. Romberg, and T. Tao, "Stable signal recovery from incomplete and inaccurate measurements," *Communications on pure and applied mathematics*, vol. 59, no. 8, pp. 1207–1223, 2006.

[3] D. L. Donoho, "Compressed sensing," *IEEE transactions on Information Theory*, vol. 52, no. 4, pp. 1289–1306, 2006.

[4] M. Lustig, J. M. Santos, D. L. Donoho, and J. M. Pauly, "$k-t$ SPARSE: High frame rate dynamic MRI exploiting spatio-temporal sparsity," in *Proc. of the 13th Annual Meeting of ISMRM, Seattle*, vol. 2420, 2006.

[5] U. Gamper, P. Boesiger, and S. Kozerke, "Compressed sensing in dynamic MRI," *Magnetic Resonance in Medicine*, vol. 59, no. 2, pp. 365–373, 2008.

[6] H. Jung, K. Sung, K. S. Nayak, E. Y. Kim, and J. C. Ye, "k-t FOCUSS: A general compressed sensing framework for high resolution dynamic MRI," *Magn. Reson. Med.*, vol. 61, no. 1, pp. 103–116, 2009.

[7] R. Otazo, D. Kim, L. Axel, and D. K. Sodickson, "Combination of compressed sensing and parallel imaging for highly accelerated first-pass cardiac perfusion MRI," *Magnetic Resonance in Medicine*, vol. 64, no. 3, pp. 767–776, 2010.

[8] S. G. Lingala, Y. Hu, E. DiBella, and M. Jacob, "Accelerated dynamic MRI exploiting sparsity and low-rank structure: k-t SLR," *IEEE Transactions on Medical Imaging*, vol. 30, no. 5, pp. 1042–1054, 2011.

[9] M. Usman, C. Prieto, T. Schaeffter, and P. Batchelor, "k-t group sparse: A method for accelerating dynamic MRI," *Magnetic Resonance in Medicine*, vol. 66, no. 4, pp. 1163–1176, 2011.

[10] A. Majumdar, R. K. Ward, and T. Aboulnasr, "Compressed sensing based real-time dynamic MRI reconstruction," *IEEE Transactions on Medical Imaging*, vol. 31, no. 12, pp. 2253–2266, 2012.

[11] B. Zhao, J. P. Haldar, A. G. Christodoulou, and Z.-P. Liang, "Image reconstruction from highly undersampled (k, t)-space data with joint partial separability and sparsity constraints," *IEEE Transactions on Medical Imaging*, vol. 31, no. 9, pp. 1809–1820, 2012.

[12] R. Otazo, L. Feng, H. Chandarana, T. Block, L. Axel, and D. K. Sodickson, "Combination of compressed sensing and parallel imaging for highly-accelerated dynamic MRI," in *Biomed. Imaging (ISBI), 2012 9th IEEE International Symposium on*. IEEE, 2012, pp. 980–983.

[13] L. Feng, R. Grimm, K. T. Block, H. Chandarana, S. Kim, J. Xu, L. Axel, D. K. Sodickson, and R. Otazo, "Golden-angle radial sparse parallel MRI: Combination of compressed sensing, parallel imaging, and golden-angle radial sampling for fast and flexible dynamic volumetric MRI," *Magnetic Resonance in Medicine*, vol. 72, no. 3, pp. 707–717, 2014.

[14] B. Trémoulhéac, N. Dikaios, D. Atkinson, and S. R. Arridge, "Dynamic MR image reconstruction–separation from undersampled (k, t)-space via low-rank plus sparse prior," *IEEE Transactions on Medical Imaging*, vol. 33, no. 8, pp. 1689–1701, 2014.

[15] R. Otazo, E. Candès, and D. K. Sodickson, "Low-rank plus sparse matrix decomposition for accelerated dynamic MRI with separation of background and dynamic components," *Magnetic Resonance in Medicine*, vol. 73, no. 3, pp. 1125–1136, 2015.

[16] J. Schlemper, J. Caballero, J. V. Hajnal, A. N. Price, and D. Rueckert, "A deep cascade of convolutional neural networks for dynamic MR image reconstruction," *IEEE Transactions on Medical Imaging*, vol. 37, no. 2, pp. 491–503, 2018.

[17] S. G. Lingala and M. Jacob, "Blind compressive sensing dynamic MRI," *IEEE transactions on medical imaging*, vol. 32, no. 6, pp. 1132–1145, 2013.

[18] Y. Wang and L. Ying, "Compressed sensing dynamic cardiac cine MRI using learned spatiotemporal dictionary," *IEEE transactions on Biomedical Engineering*, vol. 61, no. 4, pp. 1109–1120, 2014.

[19] J. Caballero, A. N. Price, D. Rueckert, and J. V. Hajnal, "Dictionary learning and time sparsity for dynamic MR data reconstruction," *IEEE Transactions on Medical Imaging*, vol. 33, no. 4, pp. 979–994, 2014.

[20] H. Yoon, K. S. Kim, D. Kim, Y. Bresler, and J. C. Ye, "Motion adaptive patch-based low-rank approach for compressed sensing cardiac cine MRI," *IEEE Transactions on Medical Imaging*, vol. 33, no. 11, pp. 2069–2085, 2014.

[21] K. H. Jin, D. Lee, and J. C. Ye, "A general framework for compressed sensing and parallel MRI using annihilating filter based low-rank Hankel matrix," *IEEE Transactions on Computational Imaging*, vol. 2, no. 4, pp. 480–495, 2016.

[22] E. J. Candès, J. Romberg, and T. Tao, "Robust uncertainty principles: Exact signal reconstruction from highly incomplete frequency information," *IEEE Trans, on Inf. Theory*, vol. 52, no. 2, pp. 489–509, 2006.

[23] M. Lustig, D. Donoho, and J. M. Pauly, "Sparse MRI: The application of compressed sensing for rapid MR imaging," *Magnetic Resonance in Medicine*, vol. 58, no. 6, pp. 1182–1195, 2007.

[24] H. Jung, J. C. Ye, and E. Y. Kim, "Improved k–t BLAST and k–t SENSE using FOCUSS," *Physics in medicine and biology*, vol. 52, no. 11, p. 3201, 2007.

[25] R. Ahmad, H. Xue, S. Giri, Y. Ding, J. Craft, and O. P. Simonetti, "Variable density incoherent spatiotemporal acquisition (VISTA) for highly accelerated cardiac MRI," *Magnetic Resonance in Medicine*, vol. 74, no. 5, pp. 1266–1278, 2015.

[26] S. Li, Y. Zhu, Y. Xie, and S. Gao, "Dynamic magnetic resonance imaging method based on golden-ratio cartesian sampling and compressed sensing," *PloS one*, vol. 13, no. 1, p. e0191569, 2018.

[27] B. Gözcü, R. K. Mahabadi, Y.-H. Li, E. Ilıcak, T. Çukur, J. Scarlett, and V. Cevher, "Learning-based compressive MRI," *IEEE Transactions on Medical Imaging*, 2018.

[28] S. Ravishankar and Y. Bresler, "MR image reconstruction from highly undersampled k-space data by dictionary learning," *IEEE Transactions on Medical Imaging*, vol. 30, no. 5, pp. 1028–1041, 2011.

[29] L. Feng, L. Axel, H. Chandarana, K. T. Block, D. K. Sodickson, and R. Otazo, "XD-GRASP: Golden-angle radial MRI with reconstruction of extra motion-state dimensions using compressed sensing," *Magnetic Resonance in Medicine*, vol. 75, no. 2, pp. 775–788, 2016.

[30] D. Kim, H. A. Dyvorne, R. Otazo, L. Feng, D. K. Sodickson, and V. S. Lee, "Accelerated phase-contrast cine MRI using k-t SPARSE-SENSE," *Magnetic Resonance in Medicine*, vol. 67, no. 4, pp. 1054–1064, 2012.

[31] L. Weizman, Y. C. Eldar, and D. Ben Bashat, "Compressed sensing for longitudinal MRI: An adaptive-weighted approach," *Medical physics*, vol. 42, no. 9, pp. 5195–5208, 2015.

[32] S. Vasanawala, M. Murphy, M. T. Alley, P. Lai, K. Keutzer, J. M. Pauly, and M. Lustig, "Practical parallel imaging compressed sensing MRI: Summary of two years of experience in accelerating body MRI of pediatric patients," in *Biomedical Imaging: From Nano to Macro, 2011 IEEE International Symposium on*. IEEE, 2011, pp. 1039–1043.

[33] H. Jung, J. Park, J. Yoo, and J. C. Ye, "Radial k-t FOCUSS for high-resolution cardiac cine MRI," *Magnetic Resonance in Medicine*, vol. 63, no. 1, pp. 68–78, 2010.

[34] S. Winkelmann, T. Schaeffter, T. Koehler, H. Eggers, and O. Doessel, "An optimal radial profile order based on the golden ratio for time-resolved MRI," *IEEE Transactions on Medical Imaging*, vol. 26, no. 1, pp. 68–76, 2007.

[35] F. Knoll, C. Clason, C. Diwoky, and R. Stollberger, "Adapted random sampling patterns for accelerated MRI," *Magnetic resonance materials in physics, biology and medicine*, vol. 24, no. 1, pp. 43–50, 2011.

[36] Y. Zhang, B. S. Peterson, G. Ji, and Z. Dong, "Energy preserved sampling for compressed sensing MRI," *Computational and mathematical methods in medicine*, vol. 2014, 2014.

[37] J. Vellagoundar and R. R. Machireddy, "A robust adaptive sampling method for faster acquisition of MR images," *Magnetic resonance imaging*, vol. 33, no. 5, pp. 635–643, 2015.

[38] M. Seeger, H. Nickisch, R. Pohmann, and B. Schölkopf, "Optimization of k-space trajectories for compressed sensing by bayesian experimental design," *Magn. Reson. Med.*, vol. 63, no. 1, pp. 116–126, 2010.

[39] S. Ravishankar and Y. Bresler, "Adaptive sampling design for compressed sensing MRI," in *Engineering in Medicine and Biology Society, EMBC, 2011 Annual International Conference of the IEEE*. IEEE, 2011, pp. 3751–3755.

[40] D.-d. Liu, D. Liang, X. Liu, and Y.-t. Zhang, "Under-sampling trajectory design for compressed sensing MRI," in *Engineering in Medicine and Biology Society (EMBC), 2012 Annual International Conference of the IEEE*. IEEE, 2012, pp. 73–76.

[41] Z. Wang, A. C. Bovik, H. R. Sheikh, and E. P. Simoncelli, "Image quality assessment: from error visibility to structural similarity," *IEEE transactions on image processing*, vol. 13, no. 4, pp. 600–612, 2004.

[42] D. O. Walsh, A. F. Gmitro, and M. W. Marcellin, "Adaptive reconstruction of phased array mr imagery," *Magnetic Resonance in Medicine*, vol. 43, no. 5, pp. 682–690, 2000.

[43] M. A. Griswold, D. Walsh, R. M. Heidemann, A. Haase, and P. M. Jakob, "The use of an adaptive reconstruction for array coil sensitivity mapping and intensity normalization," in *International Society for Magnetic Resonance in Medicine (ISMRM), Proceedings of the 10th Scientific Meeting*, 2002, p. 2410.

[44] M. Maggioni, G. Boracchi, A. Foi, and K. Egiazarian, "Video denoising, deblocking, and enhancement through separable 4-D nonlocal spatiotemporal transforms," *IEEE Transactions on image processing*, vol. 21, no. 9, pp. 3952–3966, 2012.

[45] L. Axel and R. Otazo, "Accelerated MRI for the assessment of cardiac function," *The British journal of radiology*, vol. 89, no. 1063, p. 20150655, 2016.

APPENDIX A
INFLUENCE OF THE BATCH SIZE k ON THE MASK DESIGN

In this appendix, we further discuss the tuning of the batch size used already seen in section IV-D. We compare more batch sizes than in section IV-D and show the masks resulting from different stages of sampling. We ran the stochastic greedy algorithms with different batch sizes in the same setting of section IV-D and report on Figure 12 the PSNR of the reconstructions for the *stochastic* and the *stochastic cycling* greedy algorithms respectively. We only considered k-t FOCUSS for brevity again. As mentioned in section IV-D, unless the batch size is extremely small (less than 1% of all phase encoding lines at each greedy iteration), the results suggest that the masks obtained with Algorithms 2 and 3 yield satisfactory reconstruction quality, i.e. the same quality as the standard greedy algorithm or even an increased quality.

The Figures 13 and 14 show the different masks obtained for the batch sizes considered and several observations can be made. First of all, as expected, taking a batch size of 1 yields a totally random mask, and taking a batch size of 5 yields a mask that is more centered around the low frequencies than the one with $k = 1$ but it still spread out. Then, as the batch size increases, resulting masks seem to converge to very similar designs, but these are slightly different from the ones obtained with the standard greedy of Algorithm 1. In general, we observe that, using a batch size that is a reasonable fraction of the size of the data, the algorithm will exhibit similar performance as the original greedy algorithm.

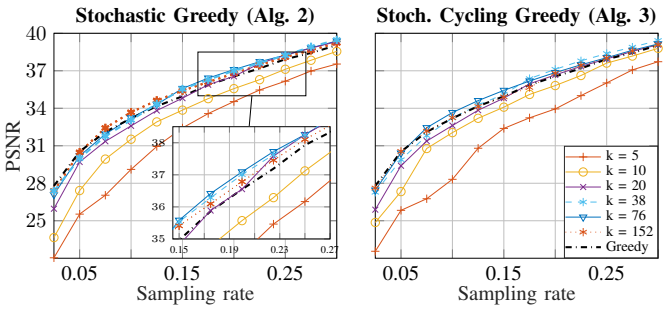

Figure 12. PSNR as a function of the sampling rate for k-t FOCUSS, comparing the effect of the batch size on the quality of the reconstruction for Algorithms 2 (on the left) and 3 (on the right). The result is averaged on 4 testing images of size $152 \times 152 \times 17$. Here, *Greedy* corresponds to the standard greedy algorithm of [27] adapted to dMRI, and is shown for comparison.

APPENDIX B
COMPARISON OF PERFORMANCES BETWEEN LB-VD AND GREEDY

In this appendix, we compare in greater detail the performances and the cross-performances of masks trained with LB-VD and Greedy. On Figure 15, we compare the LB-VD and Greedy when the trained mask is paired with its reconstruction algorithm, for a different frame than the one of Figure 5. On this Figure, we globally see that Greedy masks are able to provide a reconstruction which overall has lower errors than the one using LB-VD, which is especially noticeable on the ALOHA reconstruction, on the edge of the left ventricle.

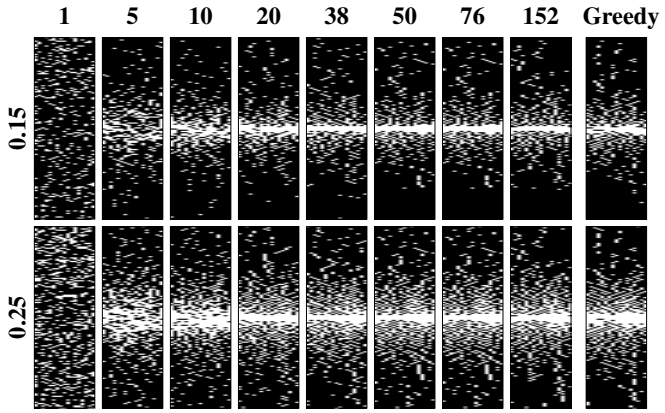

Figure 13. Learning-based masks obtained with the *stochastic* greedy algorithm (Algorithm 2) for different batch sizes k using k-t FOCUSS as a reconstruction algorithm, shown in the title of each column, for 15% (top) and 25% (bottom) sampling rate. The optimization used data of size $152 \times 152 \times 17$ with 3 training samples, with a total of 2584 possible phase encoding lines for the masks to pick from. Here, *Greedy* corresponds to the standard greedy algorithm of [27] adapted to dMRI, and is shown for comparison.

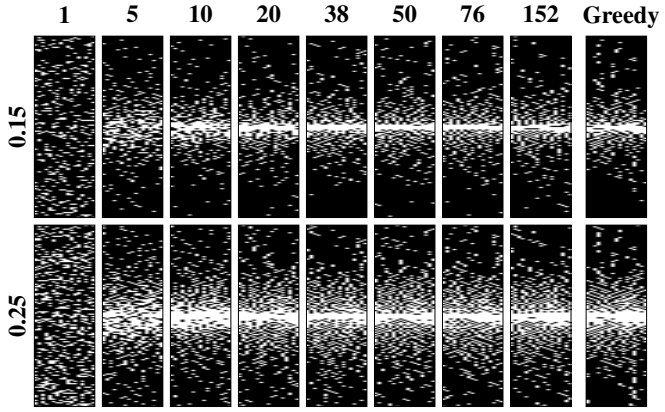

Figure 14. Learning-based masks obtained with the *stochastic cycling* greedy algorithm (Algorithm 3) for different batch sizes k using k-t FOCUSS as a reconstruction algorithm, shown in the title of each column, for 15% (top) and 25% (bottom) sampling rate. The optimization used data of size $152 \times 152 \times 17$ with 3 training samples, with a total of 2584 possible phase encoding lines for the masks to pick from. Here, *Greedy* corresponds to the standard greedy algorithm of [27] adapted to dMRI, and is shown for comparison.

The result of Figure 16 extends what was shown on Figure 4 by considering the cross-performance plots for LB-VD. A first observation is that the cross-performance of LB-VD masks does not show much variation across different algorithms: all three performances are always closely related, and usually are not able to match the performance from the greedy mask paired with the reconstruction algorithm for which it was trained. The reason for this similarity comes from the design of the LB-VD method: due to the few parameters that it has, the best parameters do not change significantly across different decoders, which results in similar masks in all cases, as shown on Figure 5, where all LB-VD masks are similar.

On the other hand, the model-free greedy approach results in widely different masks that considerably improve the reconstruction quality of the reconstruction algorithm for which it was trained.

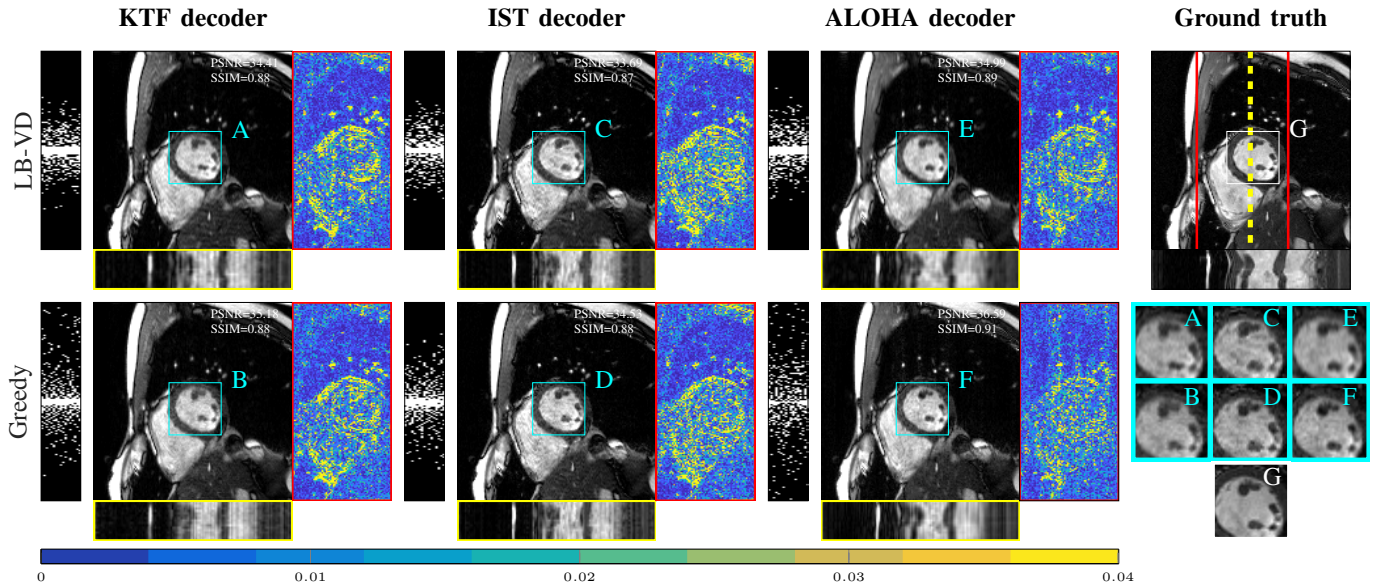

Figure 15. Extension of Figure 5, comparing LB-VD with Greedy at , for a sampling rate of 15% on a single sample with the corresponding PSNR/SSIM performances. These are images of size 152×152×17. The fourteenth frame is displayed, and the temporal profile is taken across the vertical line shown on the ground truth, and is displayed below each image.

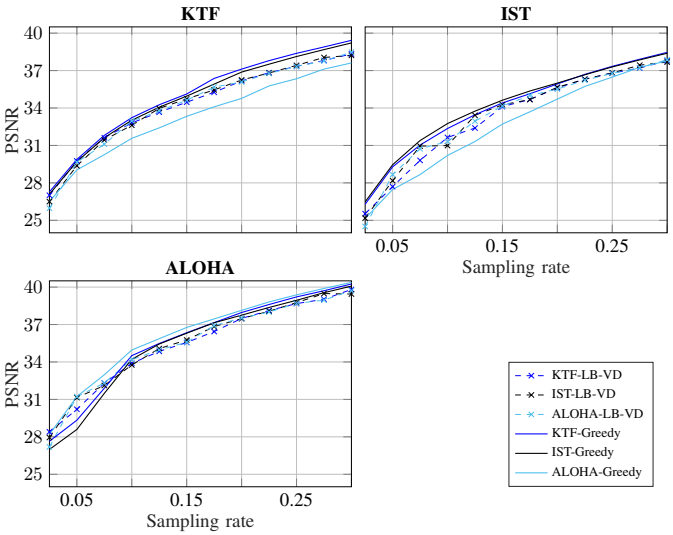

Figure 16. PSNR as a function of sampling rate for the three reconstruction algorithms considered, comparing the learning-based *greedy* result with the *Learning-based variable-density* (Algorithm 4 - optimized for each reconstruction algorithm), averaged on 4 testing images of size 152×152×17. The setting is the same as in Figure 4.

APPENDIX C
ADDITIONAL VISUAL RECONSTRUCTIONS FOR CARDIAC AND VOCAL DATASET

The present appendix provides further results for experiments IV-I and IV-J. We show in Figures 17 and 18 reconstruction at different frames which provide clearer visual information to the quality of reconstruction compared to the temporal profiles used in the article. Due to space restrictions, it was however not possible to include those along with the main numerical results.

For these images, the PSNR and SSIM are computed with respect to each individual frame, showing the quality of the reconstruction in a detailed fashion. Generally, as previously observed, the mask trained for a specific anatomy will most faithfully capture the sharp contrast transitions in the dynamic regions of the images, which is more strikingly visible on the error maps. For the vocal tract images, we notice once again in the error maps that while all learning-based methods perform relatively well, the mask obtained by our stochastic greedy algorithm using the vocal tract training dataset produces the least sharpness loss compared to the other masks.

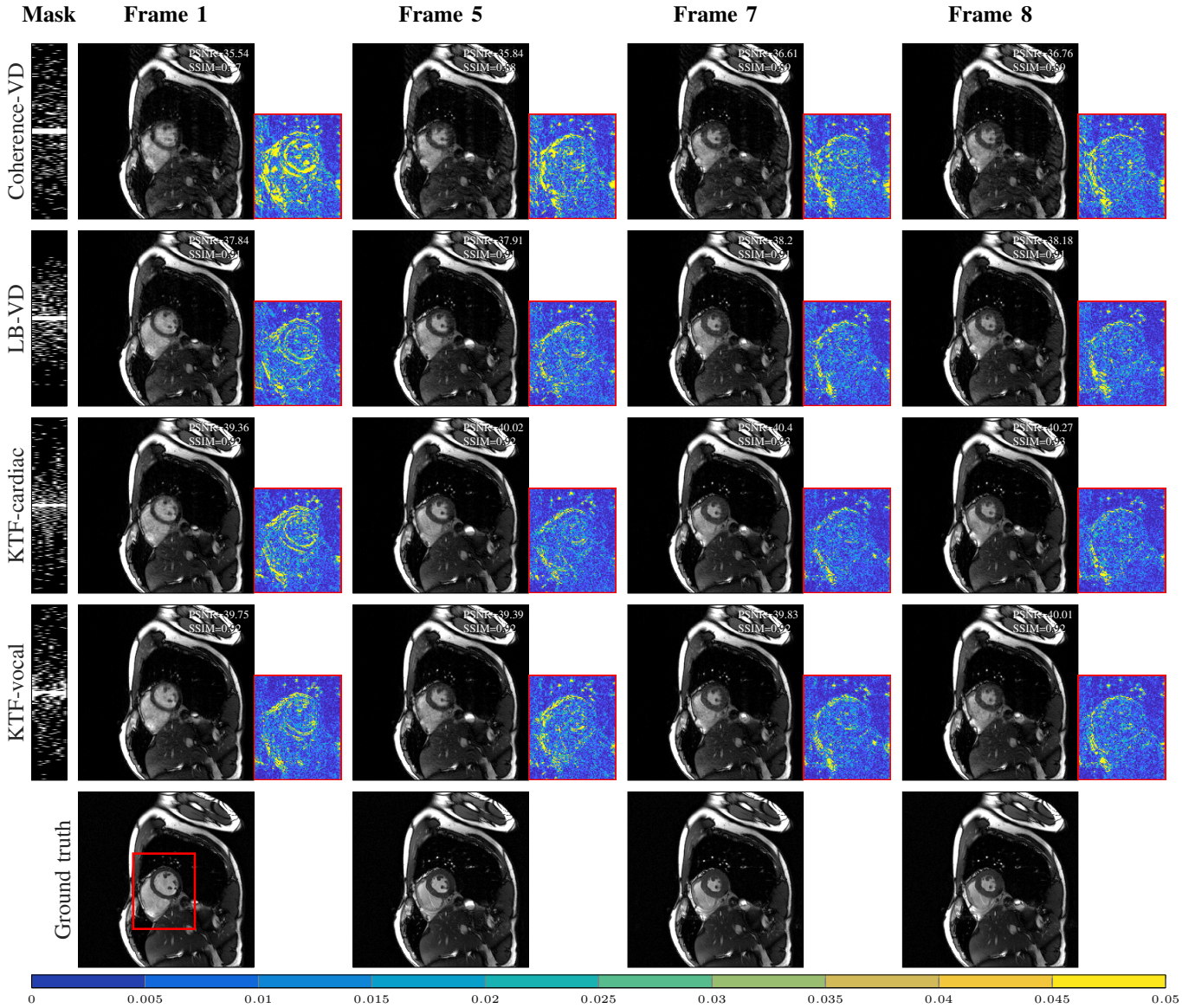

Figure 17. Reconstruction with k-t FOCUSS [6] at 15% sampling rate for the cardiac anatomy of size 256×256×10. It unfolds the temporal profile of Figure 10. The PSNR and SSIM displayed are computed for a each image, and the overall PSNR/SSIM values for all images in a sequence are given in Figure 11. The ground truth is added at the end of each line for comparison.

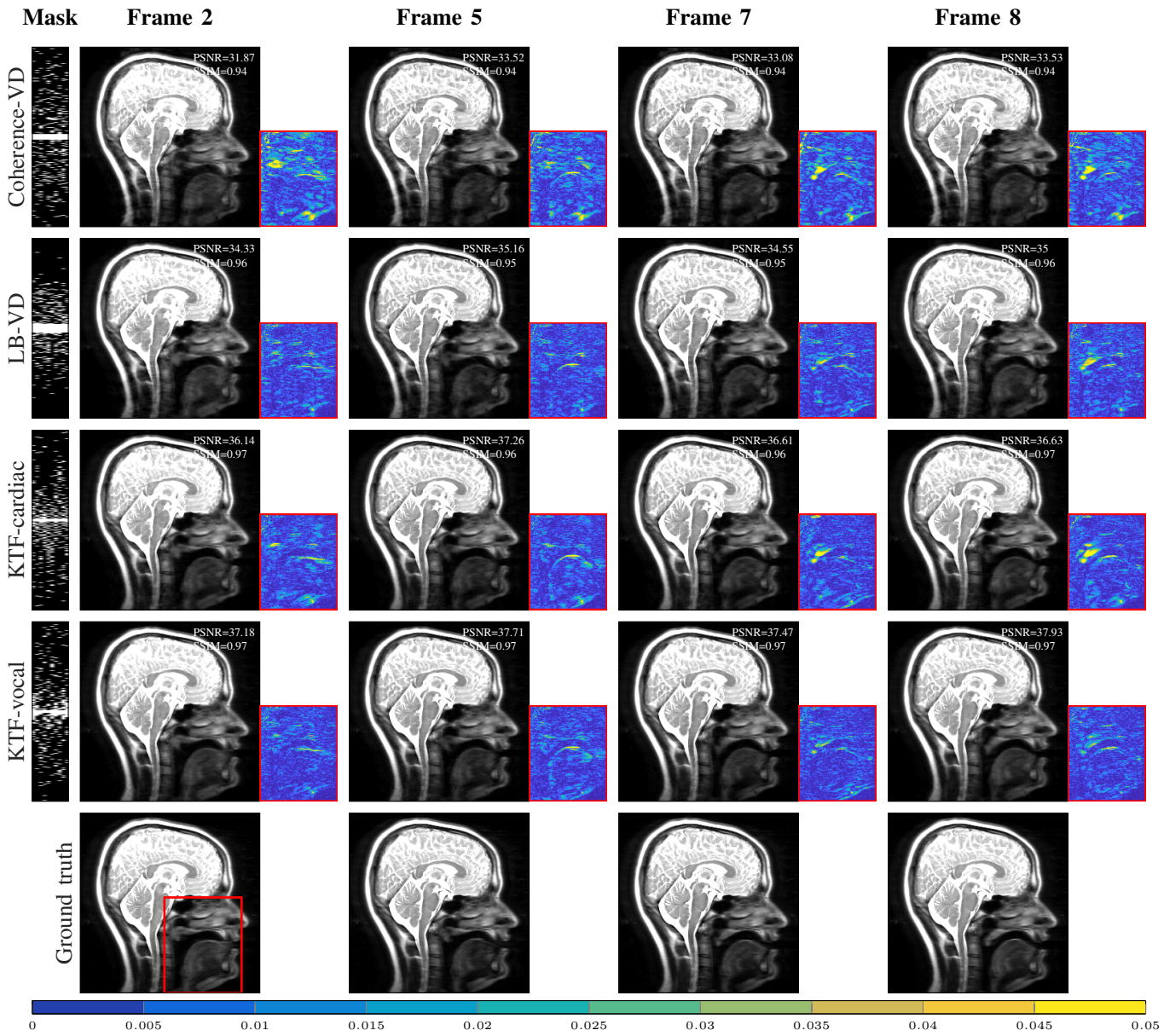

Figure 18. Reconstruction with k-t FOCUSS [6] at 15% sampling rate for the vocal anatomy of size 256×256×10. It unfolds the temporal profile of Figure 10. The PSNR and SSIM displayed are computed for a each image, and the overall PSNR/SSIM values for all images in a sequence are given in Figure 11. The ground truth is added at the end of each line for comparison.